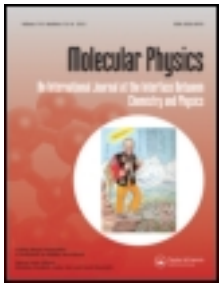

Molecular Physics: An International Journal at the Interface Between Chemistry and Physics
Publication details, including instructions for authors and subscription information:
http://www.tandfonline.com/loi/tmph20

Photoionization of tris(2-phenylpyridine)iridium

C. Nemirow [a], J. Fine [a], Z. Lu [a], K. Diri [a], A.I. Krylov [a] & C. Wittig [a]
[a] Department of Chemistry, University of Southern California, Los Angeles, CA 90089, USA

Accepted author version posted online: 03 May 2012.Version of record first published: 22 May 2012.

To cite this article: C. Nemirow, J. Fine, Z. Lu, K. Diri, A.I. Krylov & C. Wittig (2012): Photoionization of tris(2-phenylpyridine)iridium, Molecular Physics: An International Journal at the Interface Between Chemistry and Physics, 110:15-16, 1893-1908

To link to this article: http://dx.doi.org/10.1080/00268976.2012.689871

Molecular Physics
Vol. 110, Nos. 15–16, 10–20 August 2012, 1893–1908

INVITED ARTICLE

Photoionization of tris(2-phenylpyridine)iridium

C. Nemirow, J. Fine, Z. Lu, K. Diri, A.I. Krylov and C. Wittig*

Department of Chemistry, University of Southern California, Los Angeles, CA 90089, USA

(*Received 20 February 2012; final version received 18 April 2012*)

The photoionization of gas-phase tris(2-phenylpyridine)iridium ($Ir(ppy)_3$) has been examined. One- and two-photon studies yield a conservative estimate for the upper bound to the ionization energy of 6.4 eV. The one-photon experiment used 193 nm radiation. The latter experiments used tunable UV radiation to excite the ligand-centered ^{1}LC state, which is followed by radiationless decay and photoionization. An accompanying paper presents a theoretical study of excited singlets and triplets and low-energy states of $Ir(ppy)_3^+$. The calculated ionization energy is ~5.9 eV. The experimental and calculated results together indicate an ionization energy of ~6 eV. An undulation in the ion yield spectrum (~270 cm^{-1} spacing) was observed. It is due to structure in the transition that originates from T_1, which is populated through radiationless decay of ^{1}LC. At low fluence, $Ir(ppy)_3^+$ is produced without fragmentation, despite the fact that a large amount of vibrational energy is present in T_1. Specifically, this vibrational energy is the sum of $h\nu - E_{T_1}$ and the thermal energy due to the 177 $Ir(ppy)_3$ vibrational degrees of freedom at 500 K, i.e. the temperature at which the experiments were carried out. This vibrational energy is transported efficiently to the cation.

Keywords: photoionization; phosphorescence; OLED; radiationless decay; iridium complexes

1. Introduction

Electroluminescent diodes that use organic and organometallic materials are referred to as organic (organometallic) light-emitting diodes (OLEDs). Such devices and the materials that comprise them have been the subject of intense research in recent years due to potential applications, most notably in display technologies [1–5]. The optimization of a given device architecture requires attention to the many interactions that transpire within and among the constituents. In this paper the photoionization of an important OLED species, tris(2-phenylpyridine)iridium, hereafter referred to as $Ir(ppy)_3$, is examined. Introductory comments are given below to provide context for what follows. A recent review [1] and book [2] by Yersin (especially the chapter by Yersin and Finkenzeller) provide excellent overviews of the state-of-the-art of OLED research, including a number of fundamental electronic structure considerations.

A typical device consists of layers of compounds sandwiched between electrodes that inject electrons and holes into layers [1–5]. Figure 1 illustrates the most important features. A number of additional layers that further enhance device performance have been omitted to facilitate focusing on the most important processes. When a voltage is applied across the electrodes, electrons are injected from the cathode through a thin (typically $\leq$1 nm) electron injection and protection layer into the lowest unoccupied molecular orbitals (LUMOs) of molecules in the electron transport layer, which typically consists of an amorphous material such as Alq_3 (q = 8-quinolinolato-O, N) [6,7]. The injected electrons migrate slowly by directed site-to-site (polaron) hopping driven by the applied field.

The anode injects holes by removing electrons from the highest occupied molecular orbitals (HOMOs) of molecules in the hole-transport layer. The electrons and holes move toward each other under the influence of the field and form excitons in an emitter-doped recombination layer. Ideally, the excitons are highly excited states of the emitter molecules, rather than of the organic host, though the latter also can also result (ultimately) in the desired excitation [8]. Electronic excitation cascades down to the molecular excited states (indicated by an asterisk $*$) that emit photons. The photons exit via the optically transparent anode, which typically consists of a mixture of In_2O_3 and SnO_2, i.e. indium tin oxide (ITO) [4,5].

Each charge carrier has spin. In the case of a hole, the spin is that of the residual electron. Because the spins of a combining electron and hole are uncorrelated, both singlet and triplet excitons are formed. Specifically, the spins combine to give one singlet and three triplets. It is generally accepted that each of the

*Corresponding author. Email: wittig@usc.edu

ISSN 0026–8976 print/ISSN 1362–3028 online

http://dx.doi.org/10.1080/00268976.2012.689871
http://www.tandfonline.com

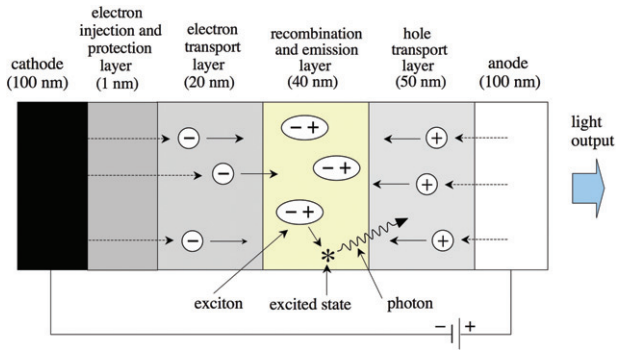

Figure 1. This schematic indicates important features of an OLED (not to scale, typical dimensions are given in parentheses). Electrons are injected from the cathode through a thin protection layer into the electron transport layer, which typically consists of an amorphous organic material. Holes are injected into the hole transport layer from an optically transparent anode (typically an In_2O_3/SnO_2 composite) that permits light to exit the device. In the recombination and emission layer, electron–hole pairs form excitons that relax to the dopant excited states (indicated by an asterisk $*$) that emit photons. Adapted from Ref. [2].

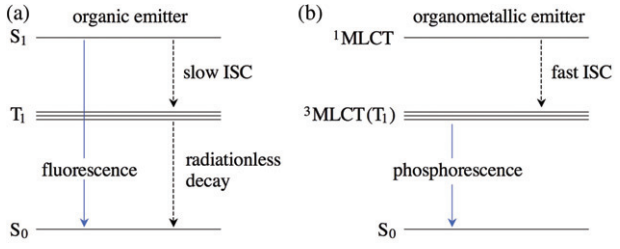

Figure 2. (a) Organic molecules (negligible spin–orbit coupling) emit only from the lowest excited singlet S_1. Because $T_1 \rightarrow S_0$ emission is extremely weak, triplet excitation is lost through radiationless decay rather than photon emission, and consequently the maximum quantum yield is 25%. (b) In triplet harvesting, electron–hole recombination leads to excitons having a triplet-to-singlet population ratio of 3:1. Excitation cascades down the triplet and singlet manifolds, with internal conversion (IC) and intersystem crossing (ISC) resulting in excitation ultimately residing in the lowest triplet, ^{3}MLCT (T_1), which emits photons. An organometallic compound (in which spin–orbit coupling (SOC) is strong) such as $Ir(ppy)_3$ experiences relatively fast ISC and efficient $T_1 \rightarrow S_0$ phosphorescence. This can result in quantum yield approaching 100%.

four states is formed with equal probability. In other words, three triplets are created for each singlet [1–3,9].

Referring to Figure 2(a), following the cascade from the initially formed excitons to lower energies, organic emitters, e.g., polyfluorenes [10], undergo fluorescence from the excited singlet S_1. Phosphorescence from the lowest triplet (whose sublevels are shown separated from one another for clarity) is, for all practical purposes, eliminated because of the long triplet spontaneous emission lifetimes that are characteristic of the weak spin–orbit coupling (SOC) regime. Because of these long spontaneous emission lifetimes, T_1 decays non-radiatively. As a result, organic emitters have low electroluminescent quantum yield [11]. In the limit of negligible $T_1 \rightarrow S_0$ emission, the maximum quantum yield is 25%.

Certain metal–ligand complexes undergo efficient phosphorescence following photoexcitation and/or the passage of electric current through solid hosts that contain these complexes [4–7,12]. As mentioned earlier, the latter means of excitation is attractive from the point of view of display technologies. Among the most promising of these complexes is $Ir(ppy)_3$ and similar species [3]. Seminal and extensive contributions by the groups of Thompson [4,12,14,15], Forrest [4,12,13,15], and Yersin [16,17] have demonstrated the high potential of this system, and promising paths to device fabrication have been identified [1,2,4–7,12,15]. Related materials can be used to obtain different emission wavelengths such that the primary colors (red, green, and blue) are obtained. For example, this tuning can be achieved by using electron withdrawing and donating groups substituted at the ppy (2-phenylpyridine) ligand [15,18].

Referring to Figure 2(b), the triplet states can be made to do useful work by employing a transition metal complex in which the transition-metal atom is responsible for strong SOC [1–3]. In such cases, the intersystem crossing (ISC) rate from ^{1}MLCT to ^{3}MLCT (T_1) is sufficiently fast to inhibit fluorescence from the lowest excited singlet [19–22]. The acronym MLCT stands for metal-to-ligand charge transfer. This label can be somewhat misleading, as the situation can be more complicated [23–25]. For the sake of brevity, hereafter we shall use the label T_1 instead of ^{3}MLCT, with the understanding that this T_1 bears no resemblance to the one in Figure 2(a), in the sense that it contains enough singlet character to ensure high phosphorescence quantum yields. As a result of efficient energy transfer processes, both singlet and triplet excitons populate the T_1 substates, which decay predominantly via phosphorescence.

This is referred to as triplet harvesting [1–3]. Strong SOC significantly increases the phosphorescence rate, enabling it to compete favorably with radiationless decay, and quantum yields therefore can approach 100% [6,12]. A number of organometallic (specifically, organo-transition-metal) complexes have been used as phosphor dopants in OLEDs to overcome the efficiency limit imposed by the absence of sufficient spin–orbit interaction [1–3,26].

Internal conversion (IC) and ISC mechanisms are enlisted frequently. Though understood separately, these are unruly in systems that consist of many potential energy surfaces (PESs), unknown coupling parameters, and condensed phase host environments, leaving open important issues: (i) electronic structure of low-lying singlets and triplets including the role of spin–orbit interaction; (ii) vibrational relaxation, e.g. from the regime of quantum chaos to that of good quantum numbers; (iii) interactions with host environments; (iv) electron–hole recombination and transport; and so on.

Not surprisingly, many singlets and triplets in the energy region of interest need to be taken into consideration. SOC is effective because of near resonances among singlets and triplets, as well as approximate symmetries. Crossings and near crossings of PESs facilitate couplings, and this likely plays an important role. For $Ir(ppy)_3$, the papers of Nozaki and Nozaki and coworkers do a good job of combining SOC with time-dependent density functional theory (TDDFT) calculations of low-lying singlets and triplets [25,27]. For example, Table 6 of Ref. [25] lists the energy, singlet fraction, and oscillator strength for 140 low-lying excited states. It is seen that spin–orbit interaction plays an important role in coupling the triplet and singlet manifolds.

To understand what happens in OLED devices, our understanding of an isolated entity such as $Ir(ppy)_3$ must evolve to one of the larger system of $Ir(ppy)_3$ plus its host. In principle, we would like to refine the theory of an isolated molecule such as $Ir(ppy)_3$ as much as possible before addressing the challenge presented by the environment. To this end, one of the most important and fundamental properties of a molecule is its ionization: vertical and adiabatic ionization energies, associated orbital and structural changes, etc. Yet, little is known about the ionization of $Ir(ppy)_3$. This is one of the factors that motivated the present study, in which the photoionization of gaseous $Ir(ppy)_3$ has been examined using a two-photon photoionization scheme in which the ligand-centered $^1LC(\pi\pi^*)$ state, hereafter referred to as ^1LC, serves as the intermediate (Figure 3). The ^1LC state is, however, an interesting intermediate in that radiationless processes (IC and ISC) rapidly transfer excitation to T_1, from which photoionization takes place. A one-photon photoionization experiment (i.e. using 193.3 nm radiation from an ArF excimer laser) was carried out as well.

Referring to Figure 3, it proved possible to isolate two-photon photoionization and characterize it over the portion of the $^1LC \leftarrow S_0$ system indicated by the yellow box. It turned out that photoionization could be achieved with no discernible ion fragmentation. In other words, at sufficiently low fluence, the parent ion, $Ir(ppy)_3^+$ dominates the mass spectrum. Large molecules such as $Ir(ppy)_3$ have high densities of electronic states at energies near and above ionization threshold, and it is not always feasible to eliminate the absorption of photons beyond the ionizing transition. In the present case, however, the very large σ_1 values (i.e. $>10^{-16}\,cm^2$ [29], see Figure 3) and, following absorption of the second photon, rapid radiationless decay in competition with ionization (discussed later) help make this possible.

From these two-photon photoionization experiments, an upper bound to the vertical ionization energy (VIE) was obtained subject to a reasonable assumption about the disposition of $Ir(ppy)_3$ vibrational energy in the $Ir(ppy)_3^+$ ion, namely that T_1 vibrational excitation is transferred more-or-less intact to the cation [31]. As mentioned above, one-photon photoionization at 193.3 nm (51,730 cm^{-1}, 6.414 eV) was also achieved. Again using the assumption that parent vibrational excitation is carried over to the cation yields an approximate upper bound of 6.4 eV. This value agrees with calculations carried out in our group, which places both the VIE and the adiabatic ionization energy (AIE) at approximately 5.9 eV, as well as a previous calculation that places the VIE at approximately 5.94 eV [32].

It is concluded that the ionization energy (both VIE and AIE) of gaseous $Ir(ppy)_3$ is in the vicinity of 6 eV. This is at odds with a value of 7.2 eV surmised from energy loss spectra, indicating the need to reinterpret the peak at 7.2 eV in the energy loss spectra [33]. It is also shown that the absorption spectrum can be reproduced rather well using vertical excitation from the S_0 equilibrium geometry. This supports the assumption that vibrational excitation is carried more-or-less intact to the cation.

In the context of applications that involve organic photovoltaics (OPVs) and OLEDs [1], a molecule's ionization energy (IE) is one of its key properties, as it quantifies a system's electron-donating ability and it is related to the reduction potential. For optimal performance of materials used in OLED devices, the IEs and electron affinities (EAs) (commonly referred to as HOMO and LUMO energies, respectively) of molecules in the active (i.e. light-generating in OLEDs and exciton-generating in OPVs) layer need to be matched to the energy levels of the electrodes. The fact that the IE of $Ir(ppy)_3$ is low augurs well for its use in OLED devices. Indeed, it is significantly lower than those of either 2-phenylpyridine (8.0 eV) [34] or a bare iridium atom (8.967 eV) [35].

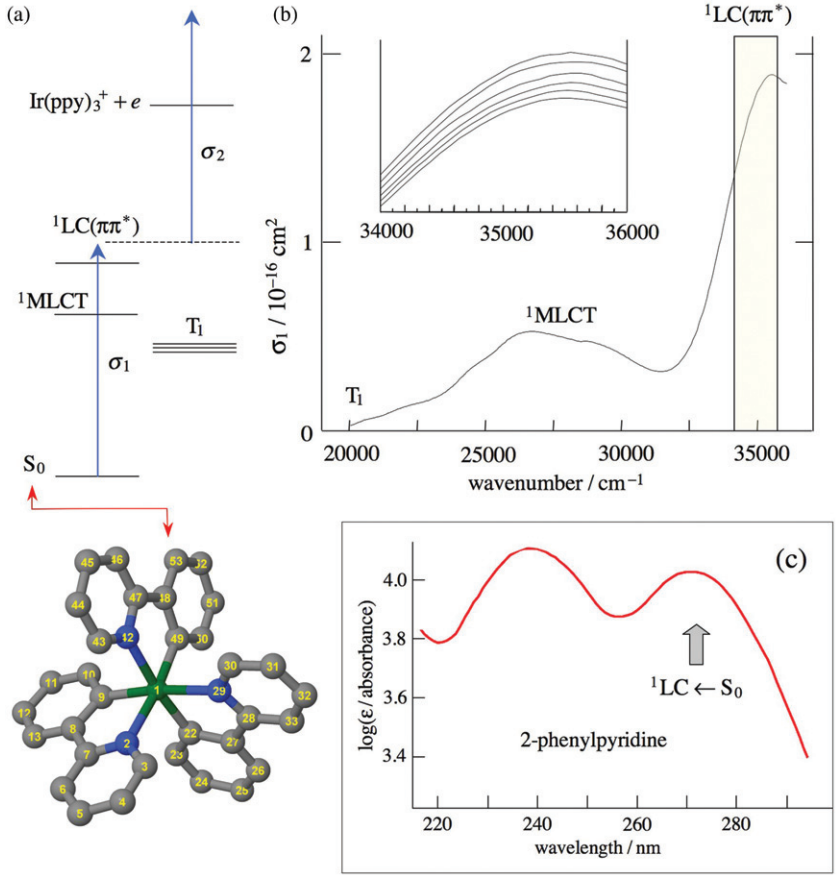

Figure 3. (a) Photoexcitation of ligand-centered $^1LC(\pi\pi^*)$ is accompanied by rapid radiationless decay: IC to ^1MLCT followed by ISC to the levels labeled T_1 (energies are not to scale) [28]. (b) Absorption spectrum of $Ir(ppy)_3$ in dimethylformamide at 414 K. Note the large σ_1 absorption cross-sections (i.e. units of $10^{-16}\,cm^2$) [29]. The yellow boxed region, 34,150–35,775 cm^{-1} (4.234–4.435 eV), corresponds to the portion of the $^1LC \leftarrow S_0$ system examined in this work. Inset: changing the temperature over the range 295–414 K has a minimal effect on the absorption spectrum in the energy range of interest; only slight broadening is observed. In order, from the top trace, the temperatures are: 295, 333, 353, 383, 408, and 414 K. The vertical axis in the inset is not labeled, as the curves are offset from one another for clarity. They are nearly identical over the indicated range. (c) Absorption spectrum of solution phase 2-phenylpyridine, adapted from Ref. [30]. The $^1LC \leftarrow S_0$ feature is analogous to the one in $Ir(ppy)_3$.

2. Experimental methods and results

The absorption spectra of $Ir(ppy)_3$ shown in Figure 3 were recorded using a Varian Cary 300 spectrophotometer. Solutions were prepared by dissolving 6 mg of $Ir(ppy)_3$ (provided by the Thompson group at USC) in 125 mL of dimethylformamide (DMF). This solvent was chosen because its high boiling point (426 K) [36] enabled spectra to be collected at temperatures up to 414 K. Spectra were also recorded using the solvent dichloromethane (DCM). Although its UV transmission is superior to that of DMF, it cannot be used at the higher temperatures because its boiling point is 313 K [36]. No significant spectral differences were observed with these solvents. Heating was achieved by wrapping the cuvettes in resistive wire and passing current through the wire. Temperature was monitored with a thermocouple.

Laser photoionization was carried out in a chamber that was evacuated using a turbomolecular pump (Leybold Turbovac 1000C), as indicated in Figure 4(a). The base pressure was 2×10^{-9} Torr. Solid $Ir(ppy)_3$ was loaded into a stainless steel cylinder and a 0.5 cm diameter aperture allowed $Ir(ppy)_3$ vapor to effuse into the chamber. The cylinder was heated using resistive wire. During operation, the cylinder temperature was maintained at approximately 500 K, and the chamber pressure was 5×10^{-9} Torr. At 500 K there was no thermal decomposition of the $Ir(ppy)_3$ sample.

Referring to Figure 4, mass spectra were recorded using a time-of-flight mass spectrometer (TOFMS).

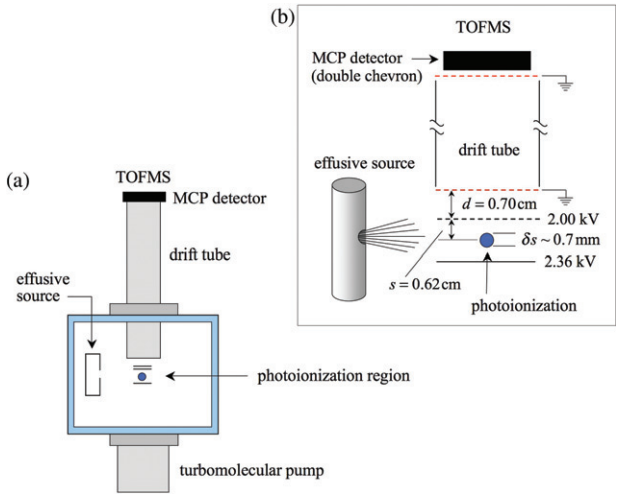

Figure 4. Schematic of the experimental arrangement. (a) The main vacuum chamber has a base pressure of 2×10^{-9} Torr. (b) Details of the time-of-flight mass spectrometer (TOFMS): Typical mass resolution was $m/\Delta m \sim 200$.

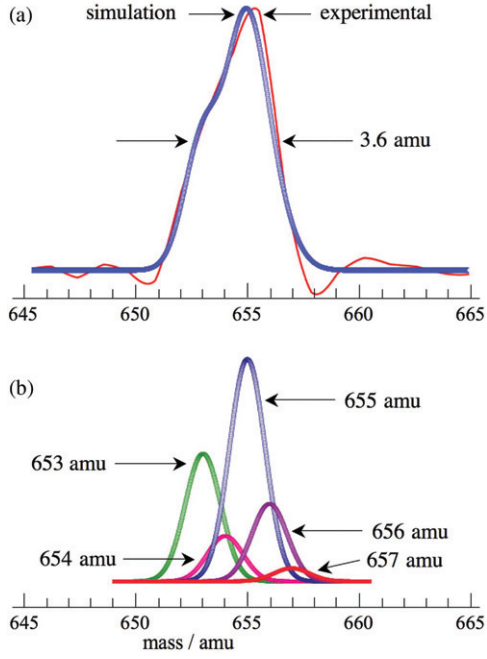

Figure 5. With 415 μJ cm^{-2} of 35,673 cm^{-1} (4.423 eV) radiation, only the Ir(ppy)$_3^+$ parent ion is observed (*vide infra* Figure 8). The Ir(ppy)$_3^+$ peak consists of contributions from the major isotopologues (see text for details). (a) The experimental curve (red) is the average of several traces, each of which is comprised of ~1000 individual spectra. The blue curve is obtained using the natural isotope abundances and assigning a 2.35 amu FWHM to each mass, as indicated in (b). This fits the experimental trace (red curve in (a)) rather well.

Photoions were produced between two electrodes: a repeller plate and an extractor that consists of a metal ring with a fine nickel mesh in the center. Ions receive an additional 2 kV of kinetic energy after passing through the extractor. They then drift for 51.3 cm before arriving at the double-chevron microchannel plate (MCP) detector. The two meshes indicated with red provide a ground shield, ensuring a field-free drift region. Calibration was carried out using NO photoionization with a variety of voltages applied to the electrodes. The NO^+ flight times, in combination with the distances indicated in Figure 4 (i.e. $d = 0.7$ cm, $s = 0.62$ cm, and $\delta s \sim 0.7$ mm), enabled the length of the drift region to be determined accurately.

Resolution was optimized at the parent ion mass by adjusting the experimental parameters to make the Ir(ppy)$_3^+$ peak as narrow as possible. Voltages of 2.36 and 2.00 kV were applied to the repeller and extractor electrodes, respectively. A voltage of approximately −1.9 kV was applied to the MCP detector. The magnitude of this voltage was increased over time to counteract degradation of the detector. Signal acquisition was carried out using a dual channel Gage Compuscope CS-8012A. The sample rate was 100 MS/s, providing 10 ns bin widths. The repetition rates were those of the lasers, 20 Hz for the two-photon studies and 10 Hz for the one-photon study. Typically, ~1000 individual spectra were summed. The TOF spectra were processed using custom Labview 8.5.1 programs to yield the mass spectra.

Under these conditions, the Ir(ppy)$_3^+$ signal shown in Figure 5(a) (solid red line) was recorded using 35,673 cm^{-1} (4.423 eV) radiation and a fluence of 415 μJ cm^{-2}. The trace shown is the average of several traces. The peak has a full width at half maximum (FWHM) of approximately 3.6 amu. A significant percentage of this width is due to the isotopic composition of the Ir(ppy)$_3$ sample. Although the natural abundance of ^{13}C is only 1.07%, Ir(ppy)$_3^+$ contains 33 carbon atoms. Consequently (rounded to the nearest tenth of a percent), 70.1% of the Ir(ppy)$_3$ molecules contain only ^{12}C atoms, 25.0% contain one ^{13}C atom, 4.3% contain two ^{13}C atoms, 0.5% contain three ^{13}C atoms, and a negligible percentage contain more than three ^{13}C atoms. Thus, ^{13}C plays a significant role in the mass spectra. Including the natural abundances of the two iridium isotopes (i.e. 62.7% and 37.3% for 193 and 191 amu, respectively) yields the following isotopologues, where the subscript on C denotes the number of ^{13}C atoms in Ir(ppy)$_3$:

^{191}Ir/^{13}C$_0$	653 amu	26.2%	^{193}Ir/^{13}C$_0$	655 amu	44.0%
^{191}Ir/^{13}C$_1$	654 amu	9.3%	^{193}Ir/^{13}C$_1$	656 amu	15.7%
^{191}Ir/^{13}C$_2$	655 amu	1.6%	^{193}Ir/^{13}C$_2$	657 amu	2.7%
^{191}Ir/^{13}C$_3$	656 amu	0.2%	^{193}Ir/^{13}C$_3$	658 amu	0.3%

The percentages of the relevant masses are 653 (26.2%), 654 (9.3%), 655 (45.6%), 656 (15.9%), 657 (2.7%), and 658 (0.3%). All but the last of these (which is negligible for the purpose of fitting the curve) are represented by the Gaussian curves indicated in Figure 5(b) that were used to fit the peak in Figure 5(a). In other words, the peak heights of the contributions in Figure 5(b) are proportional to their respective abundances. Each of the constituent peaks was assigned a FWHM of 2.35 amu. This choice is *ad hoc*. If one wishes, it can be interpreted as a rough measure of the instrumental resolution at 655 amu. Summing the curves in (b) yields the blue curve in (a), which fits the experimental data (red curve).

2.1. *Multiphoton ionization*

Photoionization was carried out using a tunable dye laser and a variety of dye mixtures to cover a reasonable portion of the $^1LC \leftarrow S_0$ system. The dye laser (Continuum HD 6000) was pumped with the second harmonic of a 10 ns, 20 Hz Nd:YAG laser (Continuum Powerlite 9020). Mixtures of rhodamine 590 and 610 (Exciton) were used. The use of these dye mixtures enabled different tuning ranges to be achieved with the kind of stable, long-term operation that is needed to obtain quantitative two-photon spectra. The dye laser output was doubled using a KDP crystal in a UV frequency extender (Continuum UVT-3), yielding radiation in the region 279–292 nm.

The laser radiation was focused using a 60 cm lens to a diameter of approximately 0.7 mm, resulting in a maximum fluence of approximately 1500 mJ cm^{-2}. The TOF spectrum obtained using this fluence and a photon energy of 35,774 cm^{-1} (4.435 eV) is shown in Figure 6. The most intense peak (i.e. the doublet centered at 192 amu) is split according to the natural isotopes of iridium. The less intense doublet centered at 204 amu is due to $^{191}IrC^+$ and $^{193}IrC^+$. Signals due to $Ir(ppy)_2^+$ and $Ir(ppy)_3^+$ (not shown) are an order of magnitude smaller than the Ir^+ peak. The cluster of peaks at lower mass is unaffected by source temperature and it is present in the absence of $Ir(ppy)_3$. Therefore, these peaks are attributed to hydrocarbon contamination.

Figure 7(a) shows the intensity of the Ir^+ signal as a function of photon energy in the range 34,900–35,800 cm^{-1} (4.327–4.438 eV). A fluence of approximately 1400 mJ cm^{-2} was used. The spectrum consists of a number of sharp peaks superimposed on a weak continuum. The only significant effect observed upon increasing the fluence is to increase the amount of underlying continuum. The boxed area in Figure 7(a) is

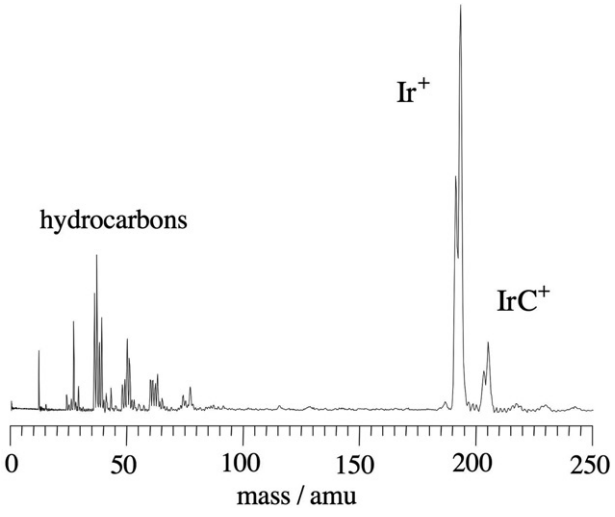

Figure 6. At a fluence of 1500 mJ cm^{-2} and photon energy of 35,774 cm^{-1} (4.435 eV), the mass spectrum is dominated by Ir^+, albeit with an IrC^+ contribution that is ~15% as large as that of Ir^+. Contributions from $Ir(ppy)_2^+$ and $Ir(ppy)_3^+$ (not

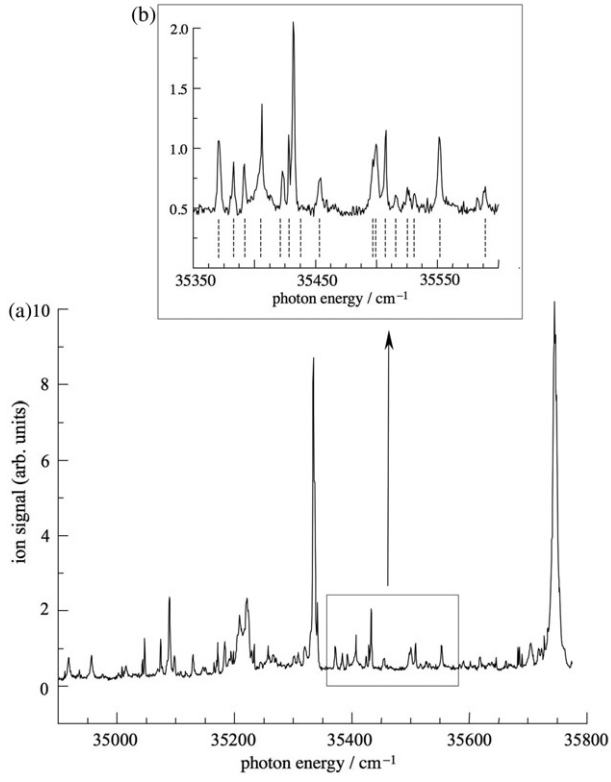

Figure 7. (a) Action spectrum obtained by monitoring Ir^+ while varying the photon energy. Laser fluence was approximately 1400 mJ cm^{-2}. (b) Expanded view: The vertical dashed lines indicate transitions of (neutral) atomic iridium [37]. Note that the spectra are not offset from zero, i.e. there is an underlying broad continuum.

expanded in (b). The vertical dashed lines correspond to transitions of neutral atomic iridium. The agreement between the measured spectrum and the dashed lines indicates that the sharp features are due to multiphoton ionization of atomic iridium [37], itself arising from multiple photon processes. In such high fluence cases, amusing spectra can be recorded, but obtaining detailed information about the low-lying excited states of $Ir(ppy)_3$ is not feasible [38].

At the same time, an important fact follows from atomic iridium spectra such as those shown in Figure 7. They indicate that, at least under high fluence conditions, photofragmentation is so severe as to yield significant quantities of iridium atoms that then undergo multiphoton ionization. In fact, neutral photofragmentation dominates. Were neutral iridium atoms produced via photodissociation of an ion precursor, there would have to be an ion partner. There is no evidence whatsoever of $Ir(ppy)^{+,}$ and only a small ppy^+ signal appears at high fluence. The dominance of neutral fragmentation channels is not surprising, given that previous studies have shown that photolysis is a common, often dominant, pathway for photoexcited organometallic compounds [39–45]. The important conclusion is that the ionization and neutral fragmentation channels are in competition with one another. This bears on the interpretation of the ion yield spectra (*vide infra* Figure 10), as discussed later.

2.2. *Two-photon ionization*

An attenuator consisting of a half-wave plate and a Glan–Thompson polarizer was inserted into the beam path. This allowed the laser fluence to be varied over a broad range with good accuracy, with the caveat that this fluence is an average over the near-Gaussian beam shape. First, the polarizer is set for maximum transmission. Then the half-wave plate is inserted between the light source and the polarizer. The fluence is easily adjusted by turning the half-wave plate. Because focusing limits the lowest fluence that can be obtained using this procedure, the focusing lens was removed to examine the low-fluence regime. In this case, the radiation passed through a 1 mm diameter aperture. This enabled a fluence as low as $50\,\mu J\,cm^{-2}$ to be achieved with good accuracy. Diffraction over the aperture–sample distance was minimal.

Figure 8 shows how changing the fluence affects the mass spectra. The highest fluence (top trace) yields a mass spectrum that is similar to the one presented in Figure 6. The Ir^+ peak dominates. Signals corresponding to $Ir(ppy)_2^+$ and $Ir(ppy)_3^+$ gain intensity as the fluence is decreased. At $88\,mJ\,cm^{-2}$, the Ir^+ and $Ir(ppy)_3^+$ peaks have approximately equal height, and an IrC_n^+/IrN_n^+ progression has emerged. When the fluence is below $\sim 1.6\,mJ\,cm^{-2}$, the $Ir(ppy)_3^+$ parent ion is isolated, i.e. the mass spectrum, for all practical purposes, contains no other peaks. No signal corresponding to $Ir(ppy)^+$ has been observed in any of the experiments.

Generally, the parent ion is most useful for acquiring information about the molecule and therefore this signal was the main focus of the present study. It should be noted that it was not obvious *a priori* that it would be possible to isolate the parent ion, particularly in light of the large amount of parent vibrational energy that is present at 500 K. Thus, it was pleasing to find that $Ir(ppy)_3^+$ was the only ion peak in the mass spectrum over a wide range of experimental conditions.

The fluence dependence of the $Ir(ppy)_3^+$ signal revealed that it is proportional to the second power of the laser fluence, as long as the fluence is less than $\sim 1.6\,mJ\,cm^{-2}$ (see Figure 8). To be on the safe side, we shall take the low-fluence regime to be less than $1\,mJ\,cm^{-2}$. Figure 9 shows a log–log plot of the $Ir(ppy)_3^+$ signal versus fluence, Φ, obtained with a

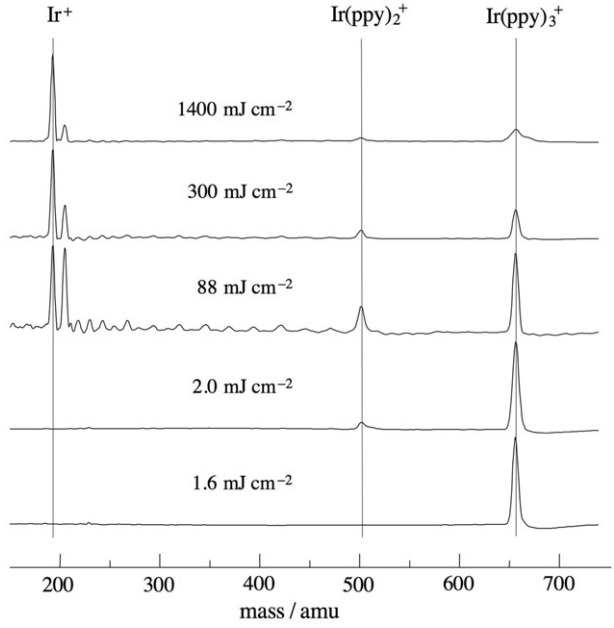

Figure 8. Mass spectra recorded at different fluences: The laser frequency is $35{,}357\,cm^{-1}$ (4.383 eV). At low fluence (bottom trace), photoionization produces the $Ir(ppy)_3^+$ ion exclusively. As the fluence is increased, fragmentation results in the appearance of the $Ir(ppy)_2^+$ ion. At high fluence (top trace), the Ir^+ peak dominates, indicating severe fragmentation of $Ir(ppy)_3$ and its photofragments.

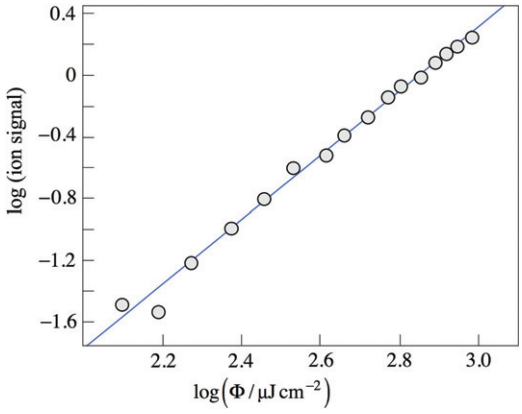

Figure 9. $Ir(ppy)_3^+$ signal versus fluence, Φ, recorded with a photon energy of 35,420 cm^{-1} (4.391 eV). The straight line has a slope of 2, in accord with two-photon ionization.

photon energy of 35,420 cm^{-1} (4.391 eV). Similar results were obtained using a number of photon energies in the range 34,207–35,930 cm^{-1} (4.241–4.455 eV). At slightly higher fluence, but below the regime where significant fragmentation occurs, the $Ir(ppy)_3^+$ signal is no longer proportional to Φ^n with $n = 2$. For example, the range 2–15 mJ cm^{-2} is characterized by $n = 1.5$. This is consistent with some degree of saturation of one or both transitions, as well as a contribution from parent ion fragmentation.

The term saturation is most often used to describe the near equality of two state populations that is brought about through the application of an intense, resonant electromagnetic field. In the system under consideration here, the electronically excited states are unstable because of radiationless decay. Therefore, the term saturation is used advisedly, i.e. to describe the regime where the figure-of-merit $\sigma\Phi$ assumes values of a few tenths or larger [46].

Figure 10(a) shows the 'fluence-corrected' $Ir(ppy)_3^+$ signal versus photon energy in the range 34,150–35,775 cm^{-1} (4.234–4.435 eV). Because the $Ir(ppy)_3^+$ signal varies as the second power of the laser fluence (Φ^2) in these experiments, care was taken to ensure that the fluence did not deviate more than 5% from 450 μJ cm^{-2}. To this end, the spectrum in Figure 10(a) is composed of six separate spectra recorded using different rhodamine 590 and 610 dye mixtures. The photon energy regions covered by the different dye mixtures are indicated using horizontal double-sided arrows. In addition, the laser fluence was recorded along with the ion signal, enabling the ion signal to be corrected for the modest change of fluence using the Φ^2 dependence. This is the above-mentioned 'fluence corrected' signal.

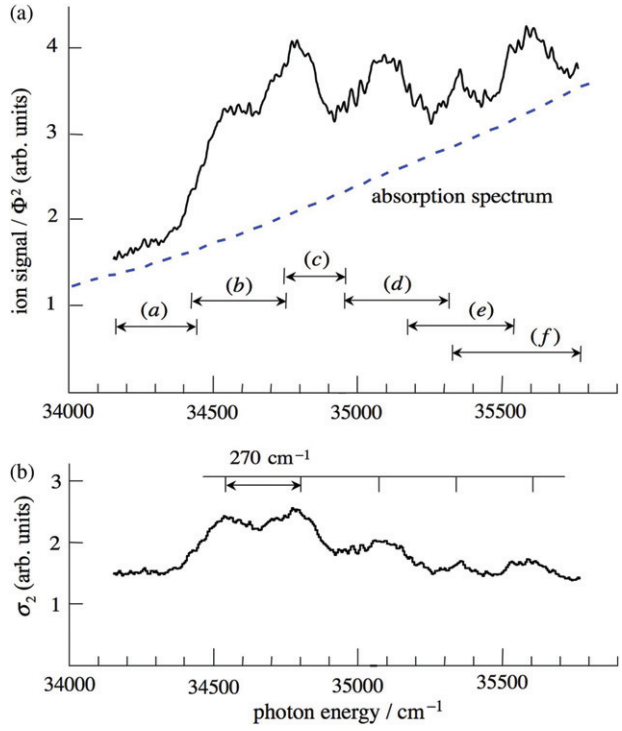

Figure 10. (a) The black trace is the $Ir(ppy)_3^+$ signal, divided by fluence squared, versus photon energy. The blue dashed trace is the absorption cross-section σ_1 of gas-phase $Ir(ppy)_3$ at ~500 K (arb. units). Different ratios of rhodamine 590 and 610 and the corresponding energy regions are designated by horizontal double-sided arrows: (*a*) 100% 590 (279.5–283.1 nm); (*b*) 590:610 = 9:1 (281.5–284.3 nm); (*c*) 590:610 = 4:1 (283.2–286.8 nm); (*d*) 590:610 = 7:3 (286.2–288.1 nm); (*e*) 590:610 = 3:2 (287.8–290.5 nm); (*f*) 100% 610 (290.2–292.8 nm). (b) The ion signal (scaled by Φ^{-2}) in (a) has been divided by the (blue dashed) absorption spectrum of ~500 K gas-phase $Ir(ppy)_3$ also shown in (a). This indicates that the undulation with ~270 cm^{-1} spacing is due to σ_2.

The trace in (b) is the black trace in (a) divided by the absorption spectrum shown as the dashed blue line in (a). An ultraviolet absorption spectrum of gaseous $Ir(ppy)_3$ was obtained by inserting a heated, sealed 10 cm cell containing $Ir(ppy)_3$ vapor into a commercial spectrophotometer. The cell was heated more at the ends than in the middle to eliminate condensation on the windows. It was wrapped in insulation and inserted into a split copper cylinder having end plates with holes just large enough to permit the radiation to enter and exit. There was no sample degradation at temperatures in excess of 550 K. Reliable ultraviolet spectra were recorded. A portion of one of them is shown in Figure 10(a). Division of the black trace in (a) by the absorption spectrum yields a spectrum (in arbitrary units) for the dependence of the ion signal on the ionizing photon energy. This is discussed in Section 3.

The upper horizontal scale in (b) indicates that the undulation has spacing of roughly 270 cm^{-1} (33 meV).

The undulation seen in Figure 10(b) was unanticipated. If anything, a smooth variation of σ_2 versus photon energy was expected [47,48]. Therefore, the photoionization spectrum shown in Figure 10 was examined thoroughly to ensure that it is not an artifact. The data were recorded with great care over several months, using six different dye solutions, ensuring that the laser fluence is safely within the two-photon regime, and taking care to not mistake a variation of laser fluence for a variation of σ_2. There was no relationship between the undulation and the tuning ranges used with the various dye mixtures. The undulation was repeatable. Possible explanations are discussed in Section 3.

2.3. *One-photon ionization*

It also proved straightforward to photoionize $Ir(ppy)_3$ using a single 193.3 nm (6.414 eV) photon. The output from an ArF excimer laser (Lambda Physik Compex 201) was passed through a 0.7 mm × 12.7 mm aperture. Less than 1 mJ cm^{-2} ($<10^{15}$ photons cm^{-2}) provided an adequate signal. No significant changes to the experimental arrangement indicated in Figure 4 were required, i.e. only optics and triggering. The sole ion present in the mass spectrum was $Ir(ppy)_3^+$. The photon energy provides an additional estimate of an upper bound for the ionization energy, subject to a reasonable assumption about the role played by parent vibrational energy in photoionization, as discussed in the next section.

3. Discussion

Referring to Figure 10, single-frequency two-photon ionization was carried out using photon energies throughout the range 34,150–35,775 cm^{-1} (4.234–4.435 eV). The two-photon nature of $Ir(ppy)_3^+$ production in this range was verified at a number of photon energies by recording data of similar quality to those shown in Figure 9. With photon energies smaller than 34,150 cm^{-1} (4.234 eV) it was not possible to obtain such high-quality fluence dependence data because the absorption cross-section σ_1 diminishes toward smaller photon energy and our ultraviolet radiation source (doubled dye laser) is less stable.

It is noteworthy that with the convenient (and significantly smaller) photon energy 28,170 cm^{-1} (3.492 eV, corresponding to 355 nm) it was not possible to identify a regime where the $Ir(ppy)_3^+$ signal varies as the square of the fluence. Even though the 355 nm radiation is quite user-friendly (being the YAG third harmonic), the photoionization fluence dependence changed erratically from one experiment to the next. For example, nine fluence dependence plots were recorded under what we considered similar conditions. In each case, the $Ir(ppy)_3^+$ signal could be fitted to a Φ^n variation. However, the n values spanned a broad range: 1.5–3.3. This was surprising because the 355 nm fluence was more stable than the radiation used throughout the range indicated in Figure 10.

As mentioned above, one of the problems is that the cross-section for absorption of the first photon (σ_1) diminishes on the low-energy side of the $^1LC \leftarrow S_0$ peak indicated in Figure 3. Consequently, increasing the fluence to overcome smaller values raises the possibility of beginning to saturate the σ_2 transition. Of course, the major unknown with 355 nm radiation is the participation of three-photon processes, as 28,170 cm^{-1} (3.492 eV) is quite a bit smaller than 34,150 cm^{-1} (4.234 eV). For example, might 355 nm photoionization be, at least in part, a three-photon process with some degree of saturation (at times) of the σ_2 and σ_3 transitions? As pointed out by one of the reviewers, competition between two- and three-photon processes can be exacerbated by the mode hopping that occurs in YAG lasers that are not injection seeded.

In consideration of the above issues, to be on the safe side, all of the spectral scans were limited to the range shown in Figure 10. Thus, 34,150 cm^{-1} (4.234 eV) was used to estimate a *very conservative* upper bound for the ionization threshold obtained via single-frequency two-photon ionization, as discussed below.

3.1. *Low-lying electronically excited states*

Insight into energy transfer and photophysical properties of low-lying electronically excited states of $Ir(ppy)_3$ is provided by previous experimental studies. The ones most germane to the present study are reviewed here.

It is well known that $Ir(ppy)_3$ exhibits intense (i.e. high quantum yield) phosphorescence from T_1 with an apparent radiative (spontaneous emission) lifetime of approximately 1.6 μs at room temperature [16,17,20,24,28]. This lifetime is phenomenological in the sense that the three T_1 sublevels separately have quite different radiative lifetimes: 116, 6.4, and 0.2 μs, as indicated in Figure 11 [17]. It is interesting that the term phosphorescence is used with a radiative lifetime as short as 0.2 μs. Specifically, 0.2 μs is comparable to the spontaneous emission lifetimes of a large number of allowed singlet–singlet transitions in small

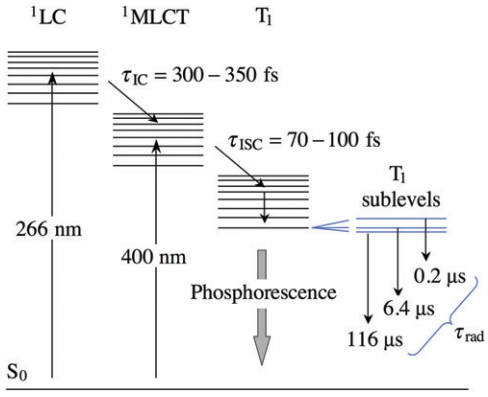

Figure 11. Some important properties and processes of low-lying electronic states are indicated schematically (not to scale). Rapid radiationless decay processes (IC and ISC, with respective lifetimes τ_{IC} and τ_{ISC}) ensure efficient T_1 production [28]. Spontaneous emission lifetimes (τ_{rad}) for the T_1 sublevels indicated on the far right differ considerably, despite the fact that these levels are close in energy, i.e. 116, 6.4, and 0.2 μs for 19,693, 19,712, and 19,863 cm^{-1}, respectively, in CH_2Cl_2 solvent [17]. At room temperature, an observed phosphorescence lifetime of 1.6 μs reflects the complex interplay that exists between the T_1 levels. The horizontal lines (above the electronic origins) whose spacing decreases with energy indicate (schematically) vibrational levels. Adapted from Refs. [17,28].

molecules. Keep in mind, however, that so short a lifetime does not, by itself, imply dominant singlet character of the excited state. Specifically, a lifetime of 0.2 μs can arise through the introduction of even modest amounts of ^{1}LC and/or ^{1}MLCT character into T_1 via SOC.

Because of the short $^1LC \rightarrow S_0$ and $^1MLCT \rightarrow S_0$ spontaneous emission lifetimes (recall the large absorption cross-sections indicated in Figure 3), only a modest percentage of ^{1}LC and/or ^{1}MLCT character is needed to account for the 0.2 μs lifetime. For example, an estimate of ~6 ns was obtained for the $^1MLCT \rightarrow S_0$ radiative lifetime. This was achieved through application of a Strickler–Berg analysis [49,50] to several molecules having similar spectral properties in the region of interest [30,51–53], and then scaling these lifetimes to the absorption spectrum shown in Figure 3 [29]. This confirmed that only a few percent of ^{1}MLCT character mixed into the T_1 state is needed to account for the short lifetime of 0.2 μs.

The radiative and energy transfer processes that transpire among the three T_1 sublevels are subtle. For example, the different spontaneous emission rates participate in proportion to the respective sublevel populations, which in turn depend on both the temperature and the energy transfer rates among the sublevels. This has been examined assiduously by Yersin and coworkers [16,17], who have established, through numerous and sophisticated experiments and modeling, the various energy transfer and radiative properties [16,17]. Specifically, in their experiments, emission spectra and decay rates (for T_1 sublevels) were recorded at temperatures as low as 1.5 K and with applied magnetic fields as high as 12 T. Suffice it to say that, leaving aside for the moment a detailed assignment of the electronic character of all low-lying singlets and triplets, the radiative and energy transfer processes of the T_1 sublevels are well understood compared with other $Ir(ppy)_3$ photophysical and energy transfer processes.

It must be kept in mind that non-radiative relaxation processes such as $^1LC \rightarrow {}^1MLCT$ and $^1MLCT \rightarrow T_1$, which appear commonly in the literature, are highly simplified (in a sense phenomenological) models. For example, in reality there are several triplets whose energies lie below that of ^{1}LC, as well as surface crossings. Details of the electronic structure are discussed at length in the accompanying (following) paper, hereafter referred to as Paper II [54].

With the above caveat in mind, at energies above the T_1 origin region (Figure 11), the femtosecond resolution transient absorption measurements of Tang *et al.* have revealed ultrafast dynamics among the ^{1}LC, ^{1}MLCT, and T_1 states [28]. Referring to Figures 3 and 11, ultrafast (100 fs) photoexcitation at 400 nm was used to access ^{1}MLCT. It was found that absorptions at 520 and 580 nm appeared with time constants of 100 fs and 70 fs, respectively. These 520 and 580 nm absorptions remained constant up to the maximum achievable delay (for the given experimental arrangement) of 1.5 ns. The long-lived absorbing state was assigned to phosphorescent T_1, implicating rapid ISC (i.e. τ_{ISC} values of 100 fs and 70 fs), as indicated in Figure 11. This result is consistent with the essentially complete absence of $^1MLCT \rightarrow S_0$ fluorescence that has been noted [17,20], even at low temperatures [17].

Next, ^{1}LC was excited at 266 nm, and the transient absorptions at 520 and 580 nm, each originating from T_1, were fit using a bi-exponential function [28]. With the shorter time constants fixed at the τ_{ISC} values (100 fs and 70 fs, respectively), the other time constants were found to be 300 fs and 350 fs, respectively (Figure 11). These longer time constants were assigned to IC from ^{1}LC to ^{1}MLCT, i.e. τ_{IC} in Figure 11. The bottom line is that this study demonstrated that photoexcited $Ir(ppy)_3$ relaxes via ^{1}MLCT to phosphorescent T_1 on a sub-picosecond timescale. Complementary experiments by Hedley *et al.* used ultrafast methods to probe directly the short-lived ^{1}MLCT spontaneous emission that follows

photoexcitation at 400 nm with 100 fs pulses [20]. These challenging experiments confirmed the results of Tang *et al*. [28], and also revealed rapid vibrational energy transfer processes, including intramolecular vibrational redistribution. Again, as impressive as these measurements are, one must keep in mind that the electronic structure is more complex that the simplified scheme indicated in Figure 11.

In the gas-phase environments of the experiments reported herein, an $Ir(ppy)_3$ molecule's energy is conserved (until it emits a photon) following its absorption of a single ultraviolet photon. Therefore, intramolecular processes take place at, for all practical purposes, fixed energies, i.e. the photon energy plus a given molecule's (considerable) internal, that arises from 490 K thermal equilibrium. This differs from the condensed phase environments that have been used in previous studies of laser-initiated dynamics in the $Ir(ppy)_3$ system. In these latter cases, intramolecular processes take place simultaneously with $Ir(ppy)_3$–host interactions. It is safe to assume that processes that take place on time scales of 70–100 fs are completely in the intramolecular regime, and processes that transpire on time scales of 300–350 fs are predominantly intramolecular. In the picosecond regime, however, it is hard to justify the assumption of solely intramolecular mechanisms, as dopant–host vibrational energy transfer processes can be competitive with intramolecular processes. When normal modes are accurate descriptors, dopant–host vibrational energy transfer will likely be slower than intramolecular processes. On the other hand, in the higher-energy regime of vibrational (vibronic) quantum chaos, dopant–host vibrational energy transfer can be rapid [55]. This regime can be accessed through IC and ISC processes.

Rapid ISC and the resulting efficient quenching of singlet–singlet fluorescence are consequences of strong (or at least efficient) SOC. Several theoretical studies have addressed this issue [23–25,27]. Of particular note are those of Nozaki [25] and Nozaki and coworkers [27], who examined effects due to SOC in $Ir(ppy)_3$ and analogous systems. The Nozaki results on $Ir(ppy)_3$ [25] are in qualitative accord with the experimental results [28].

As a result of significant singlet–triplet mixing, it has been suggested that an appropriate picture might be one in which photoexcitation produces the strongly spin-mixed phosphorescent states directly, in which case the term ISC has little meaning [25]. In other words, in a regime where ISC has little or no meaning, the lifetime τ_{ISC} would not be observed. Instead, photoexcitation would access states of mixed $^1MLCT/T_1$ character, and each of these states would emit in proportion to its percentage ^1MLCT character. This scenario differs from the case in which a temporally short pulse excites the system, with the pulse's spectral width exceeding significantly the mean energy spacing between adjacent eigenstates. A coherent superposition of eigenstates is created whose short time character is that of the 'bright state'. In the Tang *et al*. experiments (400 nm), the bright state given by this coherent superposition is ^1MLCT. This enabled τ_{ISC} to be determined.

Indeed, calculations indicate that the emitting states are of predominantly triplet character [23–25], with only modest percentages of singlet character. This is in agreement with the dilution of the very short singlet–singlet spontaneous emission rates mentioned earlier, in which T_1 acquires a small percentage of singlet character due to SOC. As a testament to the reliability of the calculations, the radiative lifetimes were reproduced, at least qualitatively, when SOC was taken into account [24]. In any event, on the basis of all of the above work [23–25], it follows that sub-picosecond ISC dynamics are not at all surprising.

3.2. *Photoionization*

Less is known about the ionization of $Ir(ppy)_3$. This is an important fundamental process that enters the world of OLEDs through the electron–hole recombination (exciton formation) that initiates the cascade down the energy 'ladder' that terminates at T_1. Yet, only one experimental value for gas-phase $Ir(ppy)_3$ appears in the literature (7.2 eV) [33], and this is based on indirect evidence, as discussed later. Properties such as the adiabatic and vertical ionization energies (AIE and VIEs) are accessible through studies of gas-phase $Ir(ppy)_3$. Ideally, one would like to prepare samples in which the $Ir(ppy)_3$ molecules have as little internal excitation as possible. However, to maintain a steady state of gas-phase $Ir(ppy)_3$ requires elevated temperature, and removing the large amount of vibrational energy imparted to the molecule at such temperatures is challenging. Even if $Ir(ppy)_3$ were somehow cooled vibrationally, considerable vibrational energy would still be implanted through the IC and ISC processes that follow and/or accompany photoexcitation. Clearly, the role played by $Ir(ppy)_3$ vibrational excitation must be taken into account.

There are two sources of vibrational excitation in the present experiments. First, consider the vibrational energy of a gas-phase $Ir(ppy)_3$ molecule at thermal equilibrium. To obtain sufficient $Ir(ppy)_3$ density in the region where photoionization takes place (Figure 6) required maintaining the oven temperature at approximately 490 K. The effusing $Ir(ppy)_3$ molecules contain

Table 1. Bond lengths (Å) for S_0, T_1, and D_0 states of $Ir(ppy)_3$.

	S_0 (theory)			S_0 (expt)			T_1 (theory)		D_0 (theory)
	(a)	(b)	(c)	(d)	(e)	(f)	(a)	(b)	(a)
$Ir–N_2$	2.168	2.153	2.167	2.088	2.071	2.132	2.196	2.176	2.149
$Ir–N_{29}$	2.169	2.154	2.167	2.088	2.071	2.132	2.175	2.169	2.184
$Ir–N_{42}$	2.165	2.151	2.167	2.088	2.071	2.132	2.139	2.116	2.213
$Ir–C_9$	2.025	2.035	2.035	2.006	2.060	2.024	2.025	2.030	2.028
$Ir–C_{22}$	2.023	2.035	2.035	2.006	2.060	2.024	2.036	2.048	1.975
$Ir–C_{49}$	2.022	2.035	2.035	2.006	2.060	2.024	1.961	2.000	2.035
$N_2–C_3$, $N_{29}–C_{30}$	1.34	1.36	–	1.345	1.361	1.331	1.34	1.36	1.34, 1.34
$N_{42}–C_{43}$	1.34	1.36	–	1.345	1.361	1.331	1.33	1.36	1.34
$N_2–C_7$, $N_{29}–C_{28}$	1.35	1.38	–	1.358	1.385	1.371	1.35	1.38	1.355, 1.35
$N_{42}–C_{47}$	1.35	1.38	–	1.358	1.385	1.371	1.40	1.439	1.35
$C_9–C_{10}$, $C_{22}–C_{23}$	1.405	1.42	–	1.405	1.374	1.401	1.40	1.42	1.395, 1.41
$C_{49}–C_{50}$	1.405	1.42	–	1.405	1.374	1.401	1.41	1.42	1.40
$C_8–C_9$, $C_{22}–C_{27}$	1.415	1.44	–	1.423	1.396	1.409	1.41	1.43	1.41, 1.407
$C_{48}–C_{49}$	1.415	1.436	–	1.423	1.396	1.409	1.49	1.485	1.426
$C_7–C_8$, $C_{27}–C_{28}$	1.47	1.47	–	–	–	1.487	1.47	1.47	1.47, 1.476
$C_{47}–C_{48}$	1.47	1.467	–	–	–	1.487	1.40	1.419	1.473

Note: (a) Current work. (b) Ref. [24]. (c) Ref. [32]. (d) Ref. [57]. (e) Ref. [58]. (f) Ref. [14].

considerable vibrational energy (discussed below) as well as, on average, $3kT/2 = 510\,cm^{-1}$ of rotational energy. As mentioned above, a second source of vibrational energy arises through the first photoexcitation step, say at $34{,}150\,cm^{-1}$ (4.234 eV). The implanted ^{1}LC excitation undergoes rapid IC to ^{1}MLCT, which in turn decays rapidly via ISC to T_1, whose origin lies at approximately $19{,}700\,cm^{-1}$ (2.442 eV) [17]. Fortunately for OLED applications, T_1 does not undergo ISC to S_0 on any relevant time scale.

The amount of vibrational energy imparted via $^1LC \leftarrow S_0$ photoexcitation is taken as the difference between the photon energy and the T_1 electronic energy, i.e. $34{,}150–19{,}700 = 14{,}450\,cm^{-1}$ (1.791 eV). Of course, vestiges of ^{1}LC and ^{1}MLCT electronic excitations remain because a gas-phase $Ir(ppy)_3$ molecule in a collision-free environment has no way other than photon emission to lower its energy. However, these contributions are minor because of the high density of T_1 vibrational states relative to the densities of vibrational states in the ^{1}LC and ^{1}MLCT manifolds at the $34{,}150\,cm^{-1}$ (4.234 eV) photon energy.

It is now assumed that vibrational excitation plays a spectator role in photoionization, i.e. all vibrational excitation in $Ir(ppy)_3$, regardless of how it got there, or the specific form it might have, appears as vibrational excitation of the $Ir(ppy)_3^+$ cation. In other words, all Franck–Condon factors between T_1 and the cation are taken as diagonal, i.e. $\langle mv_i|nv'_k\rangle = \delta_{mn}\delta_{ik}$, where i and k denote vibrational degrees of freedom such as normal modes, m and n denote numbers of quanta, and the prime denotes the ion. Note that the equilibrium geometry of the cation is quite close to that of T_1 (*vide infra* Table 1), which supports this assumption. Thus, the resulting *very conservative* upper bound to the ionization energy obtained through single-frequency two-photon ionization is estimated to be the photon energy plus the T_1 electronic energy, i.e. $34{,}150 + 19{,}700 = 53{,}850\,cm^{-1} = 6.67\,eV$.

Let us now turn to one-photon photoionization. As discussed in Section 2, it was possible to photoionize 490 K $Ir(ppy)_3$ vapor using 193.3 nm (6.414 eV) radiation. Again, if it is assumed that all vibrational excitation is transferred intact, this time from S_0 to the cation, a rough upper bound of 6.4 eV is obtained for the VIE. We shall take this to be the experimentally determined upper bound to the VIE, again subject to the assumption that parent vibrational energy is transferred more-or-less intact to the cation. Not surprisingly, it turns out that the AIE and VIEs from S_0 and T_1 geometries do not differ much from one another, as discussed below.

3.3. *Ion yield spectrum*

The two-photon $Ir(ppy)_3^+$ yield spectrum shown in Figure 10 displays an undulation whose peak-to-peak spacing is $\sim 270\,cm^{-1}$ (33 meV). As mentioned earlier, these data were recorded over several months, using six different dye solutions, ensuring that the laser fluence is safely within the two-photon regime, and taking care to not mistake a variation of laser fluence for structure

in the ion yield spectrum. Possible origins of this undulation are now discussed.

Large IC rates, such as the one determined experimentally for $^1LC \rightarrow {}^1MLCT$ [28], are consistent with non-adiabatic transitions between potential surfaces taking place via one or more conical intersections. In large systems like $Ir(ppy)_3$, the search for such intersections presents a daunting computational challenge, so much so that it is not clear that the benefit merits the effort. Nonetheless, it is well known that this is a common and efficient mechanism for the IC of electronically excited states that can leave a fingerprint in the form of selective vibrational excitation in one or more modes. In general, this could be manifest in the first and/or second photoexcitation steps, accounting for the observed structure, as discussed below.

When the two-photon ion yield spectrum shown in Figure 10 was recorded, we could not, at that time, rule out the possibility that the energy dependence of the cross-section for absorption of the first photon, $\sigma_1(E)$, is responsible for the structure. There was no report in the literature of an ultraviolet absorption spectrum of either gaseous $Ir(ppy)_3$ or even gaseous 2-phenylpyridine. Although spectra of these species in solvent display no hint of structure in the region of interest (Figure 3), this does not guarantee that the corresponding gas-phase spectra are also smooth. This led to the experiments described in Section 2, in which $\sigma_1(E)$ was measured for gas-phase $Ir(ppy)_3$ at temperatures >500 K. No undulation resembling that in Figure 10 was discernible in $\sigma_1(E)$. This confirmed that $\sigma_1(E)$ is not responsible for the undulation in the two-photon ion yield spectrum.

A likely origin of the undulation is competition between the ionization and radiationless decay pathways. In light of the fact that $^1LC \leftarrow S_0$ photoexcitation leads (via the ^1MLCT intermediate) to T_1 on a sub-picosecond timescale, the absorption of the second photon can take place via one or more predominantly triplet–triplet transitions, with T_1 being the lower state. It is unlikely that the excited state thus produced fluoresces to any significant extent. Rather, it is expected to either ionize or undergo IC and/or ISC. As mentioned above, a signature of IC via conical intersection is selective vibrational excitation, and it is likely that efficient ISC behaves similarly. Even if the photoionization cross-section has no such structure, such a mechanism – radiationless decay in competition with ionization – can account for the spectrum in Figure 10.

Given such possibilities, including combinations thereof and other scenarios, we are remiss to speculate further on the origin of the undulation indicated in Figure 10.

3.4. *Disposition of vibrational energy*

We have seen that the photoexcitation step, $^1LC \leftarrow S_0$, is accompanied by IC to ^1MLCT. At a rigorous level of theory, in the absence of molecular rotation, all molecular eigenstates in this regime are eigenfunctions of vibronic symmetry, which survives breakdown of the Born–Oppenheimer approximation [56]. However, each of these eigenstates contains only a modest amount of ^1LC electronic character, because the latter is diluted through the large density of vibrational states of the lower electronic manifold(s). Thus, as a practical matter, it is safe to assume that the system evolves to one of ^1MLCT vibrational excitation. Likewise, the $^1MLCT \rightarrow T_1$ transition that takes place via ISC also leads to mainly vibrational excitation within the T_1 manifold. Thus, the $^1LC \leftarrow S_0$ photon energy minus the energy of the T_1 electronic origin is taken as vibrational energy. Adding this to the photoexcited molecule's S_0 vibrational energy gives its total vibrational energy.

Turning now to the vibrational energy present in ground electronic state molecules, this is due to thermal population of vibrational levels at 490 K. In light of the fact that there are 177 vibrational degrees of freedom, there is considerable S_0 vibrational energy. An accurate determination of this vibrational energy distribution is challenging. The distribution function for the total amount of vibrational energy consists of (roughly) a delta function (at an energy equal to the photon energy minus the T_1 electronic energy) added to the vibrational energy distribution given by a convolution involving the 177 vibrational degrees of freedom at 490 K. This convolution yields the probability density, $P(E_{vib})$, where E_{vib} is the total vibrational energy. In plain language, the delta function accounts for the energy difference between $h\nu$ and E_{T_1}, with the assumption that the amounts of ^1LC and ^1MLCT character are small relative to that of T_1 vibrations. This distribution function is determined and discussed in Paper II.

The important point here is that essentially all of this vibrational energy is transported from T_1 to the ion, regardless of the details of its distribution. It is in this sense that vibrational excitation is said to act as a spectator in the ionization step.

3.5. *Comparison with electronic structure theory and previous work*

In Paper II, a detailed theoretical study of the electronic structure of the $Ir(ppy)_3$ system, including several low-lying states of the cation $Ir(ppy)_3^+$, is presented [54]. Here, a few of these results are

compared with the experimental findings to establish registry between the experimental and computational results.

Calculations were carried out for the AIE and for VIEs at the S_0 and T_1 geometries, yielding respective values of 5.86, 5.87, and 5.88 eV. The fact that there is little difference among these is not surprising, given the similar geometries of the S_0 and T_1 states of $Ir(ppy)_3$ and the $Ir(ppy)_3^+$ ground state, D_0 (Table 1), and the delocalized nature of the orbitals, i.e. the more delocalized the involved orbitals, the less likely it is that there will be a geometry change in going between the equilibrium structures of the electronic states. As mentioned earlier, Franck–Condon factors are expected to be nearly diagonal, where, in the present context, diagonal means $\langle mv_i|nv_k'\rangle = \delta_{mn}\delta_{ik}$, where i and k denote vibrational degrees of freedom such as normal modes, m and n denote numbers of quanta, and the prime denotes the ion. This presupposes that the normal modes of the neutral and the ion can be paired such that a given normal mode applies to both the neutral and the ion. In other words, for a given normal mode, were one to look at the classical motions of the neutral and ion they would be essentially indistinguishable. This is a good assumption in the present system. Thus, our calculations place both the AIE and the VIEs (at the S_0 and T_1 equilibrium geometries) in the vicinity of 5.9 eV. This is in accord with the experimental upper limit of 6.4 eV, and with the calculation of Hay that places the VIE at 5.94 eV [32].

To examine the assumption that vibrational energy is transferred more-or-less intact upon photoexcitation of this system, the $^1LC \leftarrow S_0$ absorption spectrum was calculated with all S_0 vibrational excitation suppressed. Excitation is vertical from the S_0 equilibrium geometry. In this calculation, 130 excited electronic states were included. Details are given in Paper II [54]. Figure 12 shows the correspondence between the calculated and experimental spectra. The shape of the experimental spectrum is reproduced, albeit with energy offset that is within the anticipated error bars of the methods employed.

It was pointed out in Section 2 that we were unable to establish that 355 nm photoionization is a two-photon process. Adding the 355 nm photon energy to the T_1 electronic energy yields 5.94 eV, which lies below the experimental upper bound of 6.4 eV, is close to our theoretical VIE and AIE values of approximately 5.9 eV, and is equal to the value calculated by Hay [32]. It may well be that our inability to establish the 355 nm photoionization fluence dependence is a reflection of this near coincidence. Thus, we conclude that the AIE is less than 6.4 eV and is most likely ~6 eV. The only other experimentally based ionization energy for this species places the VIE at 7.2 eV [33], which is incorrect. In defense of these authors, however, is the fact that their measurement was not direct, but an inference. Specifically, it was assumed that a peak at 7.2 eV in energy loss spectra (using incident electron energies of 14, 20, 30, and 50 eV) was due to ionization. Apparently this assumption needs to be reconsidered.

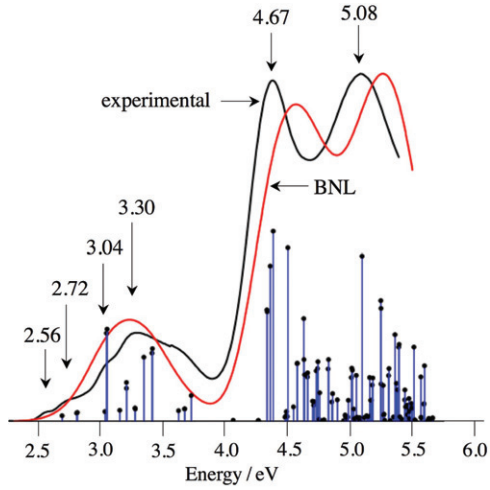

Figure 12. Ultraviolet absorption spectra of *fac*-$Ir(ppy)_3$. The calculated spectrum (red) was obtained from the stick spectrum by assigning to each stick a Gaussian FWHM of 0.43 eV. The experimental spectrum (black) was recorded at room temperature in dichloromethane. Peak and shoulder positions (vertical arrows) are in eV. All stick heights have been increased by the same constant factor for viewing convenience, and curve height has been adjusted such that the maximum absorptions are equal. The low-energy, low-intensity wing due to $T_1 \leftarrow S_0$ (2.56 eV) is absent in the calculated spectrum because SOC was not included.

4. Summary

- A regime of single-frequency two-photon photoionization has been established (i.e. below ~1 mJ cm^{-2}, see Figure 9), and it has been shown that the $Ir(ppy)_3^+$ parent ion is, for all practical purposes, the only ion product throughout this regime, despite the fact that the cation is formed with considerable vibrational energy. This is examined computationally in Paper II. Photoionization was also achieved using a single 193.3 nm (6.41 eV) photon, again yielding $Ir(ppy)_3^+$ with no discernible fragmentation.
- An upper bound for the ionization threshold for gas-phase $Ir(ppy)_3$ has been estimated on

the basis of complementary experiments. Central to interpretation of the experimental results is the reasonable assumption that $Ir(ppy)_3$ vibrational energy is carried over, essentially intact, to its ion. The two-photon experiments give a *very conservative* upper bound of 6.67 eV, while the one-photon experiment gives an upper bound of 6.4 eV. The upper bound of 6.4 eV is consistent with the theoretical values obtained by our group of approximately 5.9 eV [54] and by Hay of 5.94 eV [32]. Thus, the AIE is estimated to be ~6 eV. The VIEs at the S_0 and T_1 equilibrium geometries are essentially the same as the AIE. A calculation of the $Ir(ppy)_3$ absorption spectrum, in which vertical excitation from the S_0 equilibrium geometry is assumed, supports the assumption that vibrational excitation is transferred essentially intact upon photoexcitation.

- The electrical efficiency of an OLED depends on the embedded molecule's T_1 energy relative to its ionization energy in the solid host. For example, the IEs and electron affinities (EAs) (HOMO and LUMO energies, respectively) of molecules in the light-emitting layer needs to be matched to the energy levels of the electrodes. The low value of ~6 eV for the ionization energy of isolated $Ir(ppy)_3$ augurs well for this species and its close relatives.
- An undulation with spacing of ~270 cm^{-1} (33 meV) was observed in the $Ir(ppy)_3^+$ two-photon yield spectrum. It was shown that this is not due to such structure in the energy dependence of the absorption cross-section for the first photoexcitation step, $\sigma_1(E)$. Specifically, there is no such structure in the ultraviolet absorption spectrum of 500 K gas-phase $Ir(ppy)_3$. The most likely origin of this undulation is structure in the energy dependence of $\sigma_2(E)$. Competition between radiationless decay and ionization can play a role. Resolution of the mechanism awaits further experimental work.

Acknowledgements

The authors are pleased to acknowledge the valuable assistance of Dr. Yihan Shao from QChem, Inc. This research has been supported through grants from the National Science Foundation. The experimental work was supported by CHE-0652830 (CN, JF, ZL, and CW). The theoretical work was conducted under the auspices of the iOpenShell Center for Computational Studies of Electronic Structure and Spectroscopy of Open-Shell and Electronically Excited Species: CRIF:CRF CHE-0625419-0624602-0625237 and CHE-0951634 (AIK and KD).

References

[1] H. Yersin, A.F. Rausch, R. Czerwieniec, T. Hofbeck and T. Fischer, Coord. Chem. Rev. **255**, 2622 (2011).
[2] H. Yersin, editor, *Highly Efficient OLEDs with Phosphorescent Materials* (Wiley–VCH, Weinheim, 2008), especially H. Yersin and W.J. Finkenzeller, pp. 1–97.
[3] H. Yersin, Top. Curr. Chem. **241**, 1 (2004).
[4] M.A. Baldo, S. Lamansky, P.E. Burrows, M.E. Thompson and S.R. Forrest, Appl. Phys. Lett. **75**, 4 (1999).
[5] M. Baldo, M. Thompson and S. Forrest, Nature **403**, 750 (2000).
[6] C. Adachi, M.A. Baldo, M.E. Thompson and S.R.J. Forrest, J. Appl. Phys. **90**, 5048 (2001).
[7] C. Adachi, M. Thompson and S. Forrest, IEEE **8**, 372 (2002).
[8] C. Adachi, R.C. Kwong, P. Djurovich, V. Adamovich, M.A. Baldo, M.E. Thompson and S.R. Forrest, Appl. Phys. Lett. **79**, 2082 (2001).
[9] M.A. Baldo, D.F. O'Brien, M.E. Thompson and S.R. Forrest, Phys. Rev. B **60**, 14422 (1999).
[10] M. Leclerc, J. Polym. Sci. A: Polym. Chem. **39**, 2867 (2001).
[11] V. Cleave, G. Yahioglu, P. Le Barny, R.H. Friend and N. Tessler, Adv. Mater. **11**, 285 (1999).
[12] C. Adachi, M.A. Baldo, S.R.J. Forrest and M.E. Thompson, Appl. Phys. Lett. **77**, 904 (2000).
[13] M.A. Baldo and S.R. Forrest, Phys. Rev. B **62**, 10958 (2000).
[14] A.B. Tamayo, B.D. Alleyne, P.I. Djurovich, S. Lamansky, I. Tsyba, N.N. Ho, R. Bau and M.E. Thompson, J. Am. Chem. Soc. **125**, 7377 (2003).
[15] S. Lamansky, P. Djurovich, D. Murphy, F. Abdel-Razzaq, H. Lee, C. Adachi, P. Burrows, S.R. Forrest and M.E. Thompson, J. Am. Chem. Soc. **123**, 4304 (2001).
[16] W.J. Finkenzeller and H. Yersin, Chem. Phys. Lett. **377**, 299 (2003).
[17] T. Hofbeck and H. Yersin, Inorg. Chem. **49**, 9290 (2010).
[18] X. Liu, J. Feng, A. Ren, L. Yang, B. Yang and Y. Ma, Opt. Mater. **29**, 231 (2006).
[19] G.J. Hedley, A. Ruseckas and I.D.W. Samuel, J. Phys. Chem. A Lett. **113**, 2 (2008).
[20] G.J. Hedley, A. Ruseckas and I.D.W. Samuel, Chem. Phys. Lett. **450**, 292 (2008).
[21] G.J. Hedley, A. Ruseckas, Z. Liu, S.-C. Lo, P.L. Bum and I.D.W. Samuel, J. Am. Chem. Soc. **130**, 11842 (2008).
[22] T. Tsuboi, J. Lumin. **119/120**, 288 (2006).

[23] T. Matsushita, T. Asada and S. Koseki, J. Phys. Chem. C **111**, 6897 (2007).
[24] E. Jansson, B. Minaev, S. Schrader and H. Ågren, Chem. Phys. **333**, 157 (2007).
[25] K. Nozaki, J. Chin. Chem. Soc. **53**, 101 (2006).
[26] A.F. Rausch, H.H.H. Homeier and H. Yersin, Top. Organomet. Chem. **29**, 193 (2010).
[27] K. Nozaki, K. Takamori, Y. Nakatsugawa and T. Ohno, Inorg. Chem. **45**, 6161 (2006).
[28] K.-C. Tang, K.L. Lu and I.-C. Chen, Chem. Phys. Lett. **386**, 437 (2004).
[29] W. Holzer, A. Penzkofer and T. Tsuboi, Chem. Phys. Lett. **308**, 93 (2005).
[30] P. Krumholz, J. Am. Chem. Soc. **73**, 3487 (1951).
[31] P.M. Johnson and C.E. Otis, Annu. Rev. Phys. Chem. **32**, 139 (1981).
[32] P.J. Hay, J. Phys. Chem. A **106**, 1634 (2002).
[33] A.V. Kukhta, I.N. Kukhta, S.A. Bagnich, S.M. Kazakov, V.A. Andreev, O.L. Neyra and E. Meza, Chem. Phys. Lett. **434**, 11 (2007).
[34] K.D. Dobbs and K. Sohlberg, J. Chem. Theory Comput. **2**, 1530 (2006).
[35] Periodic Table of the Elements: http://www.periodni.com/ir.html
[36] *CRC Handbook of Chemistry and Physics,* 92nd ed. (2011–2012).
[37] T.A.M. Van Kleef, Physica **23**, 843 (1957).
[38] F.P. Ow, P.I. Djurovich, M.E. Thompson and J.I. Zink, Inorg. Chem. **47**, 2389 (2008).
[39] S.Y. Ketkov, H.L. Selzle, E.W. Schlag and G. Domrachev, J. Phys. Chem. A **107**, 4041 (2003).
[40] S.Y. Ketkov, H.L. Selzle, E.W. Schlag and S.N. Titova, Chem. Phys. **293**, 91 (2003).
[41] S. Leutwyler, U. Even and J. Jortner, J. Phys. Chem. **85**, 3026 (1981).
[42] S. Leutwyler, U. Even and J. Jortner, Chem. Phys. Lett. **74**, 11 (1980).
[43] P.C. Engelking, Chem. Phys. Lett. **74**, 207 (1980).
[44] J.E. Braun, H.J. Neusser, P. Harter and M. Stockl, J. Phys. Chem. A **104**, 2013 (2000).
[45] L. Banares, T. Baumet, M. Bergt, B. Kiefer and G. Gerber, J. Chem. Phys. **108**, 5799 (1998).
[46] V.S. Letokhov, *Laser Photoionization Spectroscopy* (Academic Press, Orlando, FL, 1987).
[47] V.S. Antonov and V.S. Letokhov, Appl. Phys. **24**, 89 (1981).
[48] M.N.R. Ashfold and J.D. Howe, Annu. Rev. Phys. Chem. **56**, 57 (1994).
[49] S.J. Strickler and R.A. Berg, J. Chem. Phys. **37**, 814 (1962).
[50] J.B. Birks and D.J. Dyson, Proc. R. Soc. Lond. Ser. A **275**, 135 (1963).
[51] H. Du, R.C.A. Fuh, J.Z. Li, L.A. Corkan and J.S. Lindsey, Photochem. Photobiol. **68**, 141 (1998).
[52] G.M. Hale and M.R. Querry, Appl. Opt. **12**, 555 (1973).
[53] J. Kubin and A. Testa, J. Photochem. Photobiol. A: Chem. **83**, 91 (1994).
[54] J. Fine, K. Diri, A.I. Krylov, C. Nemirow, Z. Lu and C. Wittig, Mol. Phys., submitted with this paper.
[55] E. Polyakova, D. Stolyarov, X. Zhang, V.V. Kresin and C. Wittig, Chem. Phys. Lett. **375**, 253 (2003).
[56] S. Ionov, H.F. Davis, K. Mikhaylichenko, L. Valachovic, R.A. Beaudet and C. Wittig, J. Chem. Phys. **101**, 4809 (1994).
[57] F.H. Allen and O. Kennard, Chem. Des. Auto. News **8**, 31 (1993).
[58] J. Breu, P. Stossel, S. Schrader, A. Starukhin, W.J. Finkenzeller and H. Yersin, Chem. Mater. **17**, 1745 (2005).